International Journal of Hydrogen Energy 103 (2025) 645–658

Contents lists available at ScienceDirect

International Journal of Hydrogen Energy

journal homepage: www.elsevier.com/locate/he

# Evolution of atomically dispersed co-catalysts during solar or UV photocatalysis for efficient and sustained $H_2$ production

Anabela Capelo [a], Domenico Fattoruso [b], Laura Carolina Valencia-Valero [b], M. Alexandra Esteves [a], Carmen M. Rangel [a], Alberto Puga [b,*]

[a] LNEG, Laboratório Nacional de Energia e Geologia, Estrada do Paço do Lumiar, 22, 1649-038, Lisboa, Portugal
[b] Department d'Enginyeria Química, Universitat Rovira i Virgili, Avinguda dels Països Catalans, 26, 43007, Tarragona, Spain

ARTICLE INFO

Handling Editor: Dr V Palma

ABSTRACT

The evolution of metal/titania photocatalysts during photocatalytic $H_2$ evolution is herein studied. Samples containing atomically dispersed Pt co-catalysts (single atoms, clusters and sub-nanoparticles) formed after calcination were compared to pre-reduced analogues mostly having metallic nanoparticles (diameters >1 nm) during ethanol photoreforming under either UV-rich irradiation or natural sunlight. Aggregation of ultra-dispersed oxidised platinum entities ($Pt^{\delta+}$) with concomitant reduction into $Pt^0$ nanoparticles (1–2 nm) was observed after UV irradiation by transmission electron microscopy (TEM), and diffuse reflectance UV–visible (DRUV-vis) and X-ray photoelectron (XPS) spectroscopies. A parallel, albeit slower, evolution trend was evidenced during solar photocatalysis. Conversely, atomically dispersed Cu co-catalyst species did not grow and became *in-situ* reduced into sub-nanometric $Cu^0$ under irradiation. Hydrogen production rates were remarkably high during initial stages of UV irradiation, and then declined to a sustained regime (≈50 and 8 mmol $g^{-1}$ $h^{-1}$ for $Pt/TiO_2$ or $Cu/TiO_2$, respectively, for up to 24 h of irradiation). Steadier solar photoreforming was observed in experiments performed in a compound parabolic collector tubular reactor (≈7.6 and 1.7 mmol $g^{-1}$ $h^{-1}$ for $Pt/TiO_2$ or $Cu/TiO_2$, respectively). Despite the non-negligible effect of co-catalyst rearrangement on activity rationalised herein, attenuated total reflectance Fourier-transform infrared (ATR-FTIR) spectroscopy measurements pre- and post-photocatalysis suggest that accumulation of strongly adsorbed degradation intermediates, chiefly acetate, is a major cause for rate decreases. Notwithstanding, this phenomenon did not result in total deactivation, so that sustained hydrogen production upon long-term irradiation was not compromised.

## 1. Introduction

The sustainability of energy and chemical industry in terms of supply security and climate change mitigation is a matter of serious concern. The use of hydrogen is being proposed as one of possible solutions to, on the one hand, overcome the excessive reliance on fossil fuel resources, and in turn, reduce global carbon dioxide emissions [1,2]. Hydrogen may become a clean and renewable energy carrier for transportation, energy supply and, moreover, as an industrial commodity [3]. Regrettably, its current uses are restricted to traditional (petro)chemical processes, chiefly crude oil refining or ammonia production [4]. Low-emissions, renewable, green hydrogen produced by electrolysis of water still represents a minor fraction (*ca.* 0.1%) of global production despite the social and political momentum it is gaining [4]. Valorisation of biomass or waste feedstocks represents an alternative option for the production of hydrogen [5]. Most of these latter routes are performed via high-temperature processes such as gasification of raw solid substrates [6,7] or by catalytic reforming of pre-processed feedstocks [7,8]. The use of sunlight energy to directly drive hydrogen production is an emerging approach [9], embodied in two main solar technologies: overall water splitting [10–12] and reforming of renewable carbon feedstocks such as biomass or solid waste [13–16]. Such processes take place under remarkably mild conditions, namely near-ambient temperature and pressure, with minimal energy input other than sunlight [13,15,17].

Photocatalytic hydrogen production from organic substances in aqueous environments, *i.e.* photoreforming, entails anaerobic degradation essentially employing only water as the oxidising agent [15]. It often proceeds at higher photonic quantum yields than overall water splitting, owing to more favourable thermodynamics [15,18]. If

* Corresponding author.
*E-mail address:* alberto.puga@urv.cat (A. Puga).

https://doi.org/10.1016/j.ijhydene.2025.01.203
Received 11 July 2024; Received in revised form 16 October 2024; Accepted 13 January 2025
Available online 22 January 2025

proceeding to completion, photoreforming results in total mineralisation with concomitant transformation into $H_2$ and $CO_2$, implying that all the chemical energy content of the initial organic matter can be recovered in the form of hydrogen as an energy carrier. This is particularly interesting in the context of energetic valorisation of aqueous waste streams such as wastewaters [19,20], or even solid waste such as plastics, biomass or food waste [13,21]. Photoreforming may also be carried out partially to obtain $H_2$ and additional oxygenated intermediates with possible value *per se* as products [14,17,22].

Most photocatalytic processes for hydrogen production are heterogeneous in nature since they rely on solid materials, generally comprising a light-responsive semiconductor and a metallic co-catalyst to promote the formation of $H_2$ [10,23,24]. Outstanding photoreforming efficiencies under UV–vis irradiation have been reported for a range of semiconductor-metal composites, among which combining $TiO_2$ with noble metal co-catalysts has proven as a robust materials design strategy [15]. Precious metals such as gold [25–29], palladium [27–30] and platinum [28,29,31–34] are reliable to furnish titania photocatalysts with efficient co-catalysts for hydrogen production using alcohols such as ethanol as model oxygenated substrates. In the case of Pt, arguably the most efficient option, unprecedented sophistication in synthetic protocols and characterisation techniques has recently prompted a flourishing research activity on atomic dispersion into single atoms or clusters, with the aim of minimising the amount of precious metal used and maximising active site accessibility [35–37]. Remarkable success has been achieved on stabilising $Pt^{\delta+}$ single atoms on $TiO_2$ [38–41], albeit they tend to evolve under UV–vis irradiation by *in-situ* reducing and aggregating into $Pt^0$ clusters and/or nanoparticles [32,40,41]. Conversely, copper is an affordable alternative that may exhibit reasonable performances [42–46]. Recent reports on atomically dispersed $Cu/TiO_2$ photocatalysts have also greatly advanced on the stabilisation of Cu single atoms and on their efficiency in hydrogen production by photoreforming [47–49]. Notwithstanding this, the achievement of high and sustained production rates is compromised by the need to increase Cu loadings, which tends to result in aggregation, and by its redox lability and the thereby ensuing dynamic leaching-deposition behaviour [42,50,51].

Beyond conflicting claims about whether platinum single atoms [39,40] or small (*ca.* 1 nm) nanoparticles [28,32] are most active for hydrogen generation, there is still some knowledge gap on the causes for the generally observed long-term activity decline of $Pt/TiO_2$ that cannot be readily explained by co-catalyst domain size [33,34]. In this work, a systematic investigation of $Pt/TiO_2$ (P-25 $TiO_2$, anatase-rutile heterojunction nanocomposite produced by flame pyrolysis) benchmark photocatalysts, both as-calcined and thermally pre-activated under $H_2$, containing either atomically dispersed $Pt^{\delta+}$ or Pt nanoparticles, in addition to as-calcined $Cu/TiO_2$, is performed to assess which are the causes for activity changes upon long-term (up to 24 h) irradiation. A thorough study on the evolution of Pt co-catalysts based on post-photocatalysis characterisation is presented, in combination with exploration of the possible effects of reaction intermediates accumulation, as hinted in previous investigations [52,53]. The scope encompasses UV irradiations in the laboratory and outdoors experiments under natural sunlight, further extended to analogous $Cu/TiO_2$ to assess the possibilities of non-precious metal alternatives. Such a comprehensive picture of the photocatalysts before and after long-term hydrogen production experiments sheds new light on how both co-catalyst morphological evolution and blockage of active sites by intermediates affect performance. Collectively, the results presented herein are particularly informative for the achievement of sustained photocatalytic hydrogen production in real and practical technologies such as those involving the use of solar reactors [54–58].

## 2. Experimental Section

### 2.1. Materials

Titanium dioxide nanopowder consisting of anatase and rutile phases (Aeroxide® $TiO_2$ P 25) was obtained as a free sample from Evonik. Hydrogen hexachloroplatinate(IV) hydrate was supplied by Fisher Scientific and used shortly after opening the bottle. Copper(II) nitrate trihydrate (puriss. p.a., 99–104%) was supplied by Sigma-Aldrich and used as received. Ultra-pure deionized water was obtained using a Milli-Q® purification system. Ethanol (p.a.) was supplied by Carlo Erba. $N_2$ (>99.999%) was supplied by Air Liquide.

### 2.2. Synthesis of photocatalysts

The initial step for the preparation of photocatalysts was done by impregnation. Typically, to a suspension of $TiO_2$ (2.0 g) in ultra-pure water (50 mL) the required amount of metallic precursor, $H_2PtCl_6{\cdot}xH_2O$ or $Cu(NO_3)_2$, was added to achieve a 1% metal/titania mass ratio and the mixture stirred at room temperature in the dark for 2 h; in the case of $H_2PtCl_6$ this was done by using an aqueous stock solution (2.5 $g_{Pt}\ L^{-1}$) after determination of its concentration by ICP (see below). Water was then removed in a rotary evaporator under reduced pressure and the solid dried until constant weight to obtain the as-prepared impregnated $Pt/TiO_2$ and $Cu/TiO_2$ materials. The second step was a calcination in a muffle furnace under static air, by applying a 2 °C $min^{-1}$ heating ramp up to 400 °C, maintaining that temperature for 2 h, and allowing to cool down to room temperature, resulting in $^{ca}Pt/TiO_2$ and $^{ca}Cu/TiO_2$ as pale ochre and pale blue solids, respectively.

One batch of the platinum/titania photocatalyst was further reduced under hydrogen at elevated temperature. In a typical procedure, a sample of ground $^{ca}Pt/TiO_2$ powder (ca. 2.0 g) was placed inside a tubular reactor and treated under a $H_2$/Ar flow (*ca.* 20:500 mL $min^{-1}$) while heating at a 10 °C $min^{-1}$ heating ramp up to 450 °C, maintaining that temperature for 3 h, and allowing to cool down to room temperature, resulting in $^{h}Pt/TiO_2$ as a grey powder. After this procedure, platinum was reduced to its metallic state and aggregated into small nanoparticles, as previously reported [32]. Schematic representations of the synthetic procedures are shown in the Supplementary Material (Fig. S1).

### 2.3. Characterisation

X-ray photoelectron spectroscopy (XPS) measurements were performed on a SPECS ProvenX-NAP instrument, using a monochromatic (μ-FOCUS 600 NAP) Al K$\alpha$ (1486.6 eV) X-ray source under ultra-high vacuum ($\approx 10^{-9}$ mbar); binding energies were referenced to the C 1s signal for adventitious organic matter at 284.8 eV. Optical absorption profiles of the photocatalytic materials were investigated by diffuse reflectance UV–vis–NIR (DRUV-vis-NIR) spectroscopy on an Agilent Cary 5000 Spectrophotometer equipped with a praying mantis sample chamber. Inductively coupled plasma optical emission spectroscopy (ICP-OES) was employed to determine the metallic concentration of Pt precursor solutions using a SPECTRO ARCOS FHS16 ICP-OES SOP spectrometer. A JEOL F200 TEM ColdFEG operated at 200 kV was used for the transmission electron microscopy (TEM) characterization, both in high-resolution transmission electron microscopy (HRTEM) and scanning transmission electron microscopy high-angle annular dark-field (STEM-HAADF) modes, coupled to energy dispersive x-ray spectroscopy (EDS) for elemental mapping and quantification. Bulk elemental compositions were determined by EDS employing an Oxford Instruments EDS Detector coupled to field-emission scanning electron microscopy (FESEM) on a Scios2 instrument. Attenuated total reflectance Fourier-transform infrared (ATR-FTIR) spectra were recorded on a Jasco FT/IR instrument. X-ray diffraction (XRD) measurements were performed on a Bruker D8 ADVANCE diffractometer. Raman spectra

were recorded using a Renishaw InVia confocal microscope at a 514 nm laser wavelength. Extended characterisation details are available in the Supplementary Material.

### 2.4. Laboratory photocatalytic experiments under UV light

Photocatalytic activity testing under UV light was performed in a photochemical borosilicate glass reactor equipped with a double quartz immersion well (Ace Glass) housing a water-refrigerated Hg vapour lamp (450 W, 325 and 574 W $m^{-2}$ for UV-A and UV-B radiations, as measured with a LP 471 UV-A and LP 471 UV-B radiation sensors, respectively) as the light source. In a typical experiment, the desired photocatalyst (125 mg) was mixed with aqueous ethanol (5 mol $L^{-1}$, 250 mL, pH ≈ 6), the pH was then adjusted to 7.0 by adding aqueous NaOH (10% *w/v*), and dispersion was ensured by ultrasonication (10 min). The suspension was transferred to the reactor vessel, heated to 40 °C, and purged with $N_2$ for 15 min before irradiation during the desired time. The generated gases were collected using a gas-tight inverted graduated burette system which allowed quantification by water displacement. Produced gas flows were additionally monitored versus time by means of a Bioprocess Control BPC® μFlow flow meter. At the end of the photocatalytic experiments, gaseous samples were taken from the burette and analysed by gas chromatography (GC) on a two channel micro-GC 3000 (Agilent), each equipped with a TCD detector, using He as the carrier gas; one channel allowed the separation and quantification of $H_2$, CO and $CH_4$ through a molecular sieve 5A column, whereas the other channel equipped with a Plot U column was used to separate and quantify $CO_2$ and light hydrocarbons. Used photocatalysts were recovered for characterisation by centrifugation-decantation, washing with water and ethanol and drying in an oven at 60 °C. Turnover frequency (TOF) values were calculated based on $H_2$ evolution rate, according to the nominal metal loading, the average metal nanoparticle size observed after irradiation (see Supplementary Material), assuming cubic fcc lattices and semi-spherical morphology and (111) facet surface atom densities.

### 2.5. Outdoors photocatalytic experiments under natural sunlight

Outdoor photocatalytic experiments under natural solar light were performed in tubular borosilicate glass reactors mounted on compound parabolic collectors at LNEG premises (Lumiar Campus, Lisbon, Portugal, approximate coordinates: 38°46′19″N, −9°10′47″W). Suspensions of photocatalysts in aqueous ethanol (5 mol $L^{-1}$) were prepared by analogous procedures to those used in the laboratory photocatalytic assays described above (0.5 g $L^{-1}$ of photocatalyst in 1.5 L), and continuously recirculated through the tubular reactor from a round bottom flask by means of a peristaltic pump (Watson Marlow SciQ 323, 100 rpm). First, the solar photocatalytic assembly was covered with a black fabric during the purging of the suspension with $N_2$ for 15 min before irradiation. After that period, the system was uncovered and subjected to solar irradiance for 3–4 h. Irradiances were measured using Delta OHM LP PYRA 03 AV, LP 471 UV-A and LP 471 UV-B radiation sensors for global, UV-A and UV-B radiation, respectively, coupled to a Delta OHM HD 2302.0 LightMeter. Reactor temperatures were estimated by employing a thermocouple probe between the collector and the tube containing the reaction mixture. The gaseous products produced were collected and measured using the inverted burette system. At the end of each experiment, the gas mixture obtained was transferred from the burette to a Tedlar® bag equipped with a valve, and analysed, to determine its composition on the micro-GC instrument as indicated above. Used photocatalysts were recovered as described above for UV experiments.

## 3. Results and discussion

### 3.1. Photocatalyst synthesis and initial characterisation

Efficiency of metal/titania materials for photocatalytic hydrogen production from alcohol substrates is remarkable in general, regardless of preparation methods and pre-activation treatments [15]. The metal component acts as a co-catalyst promoting the reductive hydrogen evolution reaction. In this regard, platinum is widely recognised as a suitable metal of robust and efficient performance [15,59], whereas copper represents a reasonably active Earth-abundant alternative, although its redox lability often results in stability issues [24,42]. In this work, both platinum/titania and copper/titania photocatalysts were prepared by an impregnation-calcination sequence. The impregnation was performed in aqueous media employing $H_2PtCl_6$ and $Cu(NO_3)_2$ as the metallic precursors, respectively. Subsequent calcination at 400 °C led to $^{ca}Pt/TiO_2$ and $^{ca}Cu/TiO_2$, which mostly contained oxidised Pt and Cu species (see section below on chemical co-catalyst evolution). The platinum/titania material was further thermally annealed at 450 °C under a hydrogen atmosphere to promote the reduction of the platinum co-catalyst, leading to $^{h}Pt/TiO_2$ (see Experimental Section for details). Basic characterisation by XRD and Raman spectroscopy indicates the expected co-existence of the anatase and rutile phases in the pristine P 25 titania support (Fig. S2).

Based on previous investigations, atomically dispersed or clustered platinum atoms are presumably ubiquitous on all titania surfaces after calcination [32,39–41]. In agreement with this, platinum is highly dispersed on all surfaces of the $^{ca}Pt/TiO_2$ photocatalyst, as revealed by STEM-HAADF (Fig. S3). To gain further qualitative and quantitative insight on Pt dispersion at the sub-nanoscale, EDS elemental maps and delimited-area X-ray emission spectra were acquired (Fig. 1). Some primary $TiO_2$ particles are densely decorated with Pt sub-nanometric particles and/or clusters, whereas others present a much lower —albeit non-negligible— Pt coverage. Platinum/titania mass ratios for either high-density or low-density coverages differ by an order of magnitude (*i.e.* 2.7 and 0.3%, respectively). The ultra-small Pt domains are barely observable on the low-density surfaces (region *2* in Fig. 1), possibly due to their fine dispersion down to sizes below the resolution limit of our non-aberration-corrected instrument. Given the atomic diameter of Pt (0.28 nm), these species are presumably clusters of very low atomicity ($Pt_2$–$Pt_4$) and single atoms [60,61]. This distribution pattern, *i.e.* well-separated and evenly distributed single atoms and clusters of different atomicity, is consistent with the category of atomically dispersed metal catalysts [35]. In the case of $^{ca}Cu/TiO_2$, copper was evenly dispersed into nanoparticles and sub-nanoparticles on the surface of titania, as observed by STEM-HAADF (see section on morphology evolution below).

The thermal treatment under hydrogen performed to transform $^{ca}Pt/TiO_2$ into $^{h}Pt/TiO_2$ caused platinum reduction and coalescence into uniformly distributed, well-separated, Pt nanoparticles of sizes around or larger than 1 nm in diameter, as clearly observed by STEM-HAADF (Fig. S3). This observation is consistent with several previous investigations [28,39,40,62–64]. Elemental mapping reveals that all platinum in $^{h}Pt/TiO_2$ is essentially concentrated in the form of nanoparticles, while little or no residual single atoms, clusters or sub-nanoparticles remain after the reductive thermal activation treatment (Fig. S3). These observations confirm that atomically dispersed or sub-nanometric platinum domains formed in $^{ca}Pt/TiO_2$ after calcination evolve into well-defined and evenly distributed nanoparticles in $^{h}Pt/TiO_2$ upon reduction by $H_2$ at 450 °C. Moreover, strong metal-support interaction upon high temperature is expected to lead to coverage of Pt nanoparticles with $TiO_x$ overlayers, possibly enhancing their stability [65,66].

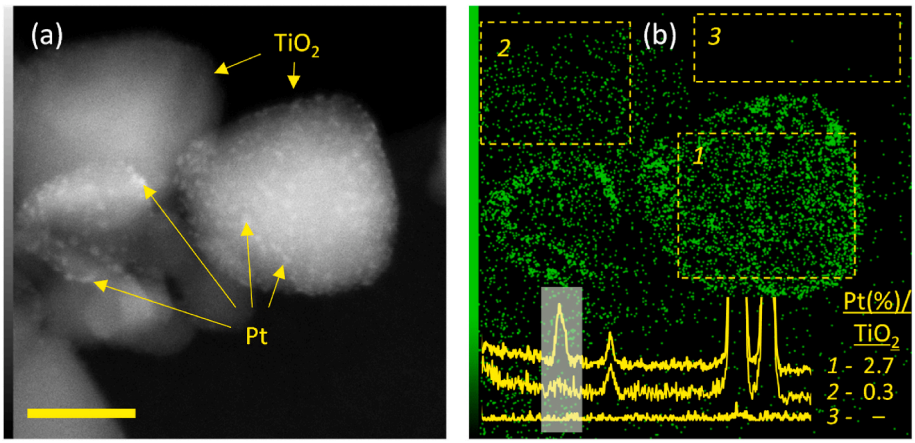


**Fig. 1.** Distribution of platinum (around or smaller than 1 nm) on titania nanoparticles (around or larger than 20 nm) in pristine $^{ca}Pt/TiO_2$ as observed by (a) STEM-HAADF and (b) elemental mapping of the same area, as obtained by EDS, showing the corresponding spectra (overlayed, shaded area marks the Pt $M_\alpha/M_\beta$ peak at *ca.* 2.1 keV, see Experimetal Section for further details) and the $Pt/TiO_2$ mass ratio (%) calculated therefrom for each of the numbered marked rectangular areas. Scale bar: 20 nm.

### 3.2. Long-term photocatalytic hydrogen production under UV light

Photocatalytic hydrogen production experiments under prolonged (24 h) intense UV irradiation were performed using both materials with platinum as the co-catalytic metal, that exhibit completely different Pt co-catalyst speciation in their as-prepared states, to assess their evolution and stability. Their gas production plots (Fig. 2a) reveal significant activity in both cases with similar kinetic behaviours, albeit at different rates. Production rates may be differentiated into two clearly distinguishable stages: remarkably rapid gas evolution is observed during short irradiation times (up to *ca.* 2 h), whereas rates suddenly declined thereafter. Although the formation of gases keeps slightly slowing down throughout the experiments, quasi-linear trends were observed during each of the stages. Average gas production rates have been determined for the initial and latter stages from the time profiles ($r_i$ and $r_f$, respectively, see Table 1). Initial rates for both $Pt/TiO_2$ photocatalysts are outstandingly high. The highest rate corresponds to $^{ca}Pt/TiO_2$ (>400 mmol $g^{-1}$ $h^{-1}$). This is rather surprising since platinum in as-calcined $^{ca}Pt/TiO_2$ is chiefly in oxidised states, and little presence of the presumably active metallic $Pt^0$ is expected. Photo-reduction of platinum surely takes place during initial irradiation [67], but the rapidity of such process in this case was unforeseen. The activated counterpart, $^{h}Pt/TiO_2$, is also highly active during initial stages, but at a lower rate (267 mmol $g^{-1}$ $h^{-1}$). Post-photocatalysis characterisation after different times is presented below and used to rationalise these unexpected observations.

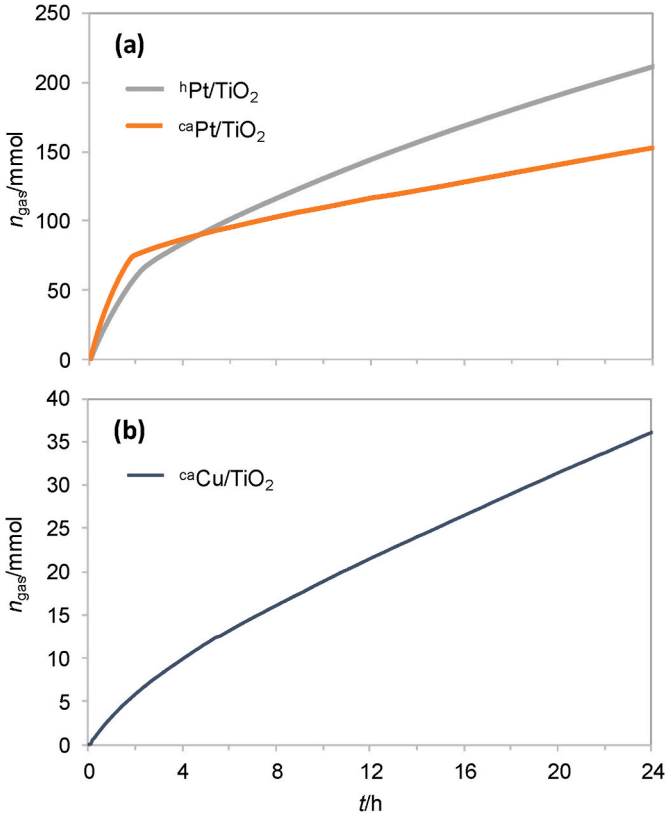


**Fig. 2.** Laboratory photocatalytic hydrogen production experiments under UV irradiation (450 W) for 24 h from aqueous ethanol (250 mL, 5 mol $L^{-1}$) suspensions of $^{h}Pt/TiO_2$ and $^{ca}Pt/TiO_2$ (a) and $^{ca}Cu/TiO_2$ (b) photocatalyst (0.5 g $L^{-1}$) at initial pH = 7, under anaerobic conditions. The cumulative amounts of gas produced are plotted *versus* time.

After the initial swift activity, the rate decline is nonetheless more abrupt for $^{ca}Pt/TiO_2$, as evidenced by the sudden change in slope of its gas production plot (see Fig. 2a and Table 1). The average gas production rate as determined after 4 h of irradiation decreased with respect to the initial by one order of magnitude (25.6 mmol $g^{-1}$ $h^{-1}$). In contrast, activity decline for $^{h}Pt/TiO_2$ is much less marked, since the volume of collected gases continues increasing more steadily at an average rate of 51.6 mmol $g^{-1}$ $h^{-1}$ (Fig. 2a–Table 1). This indicates that the reductively and thermally pre-reduced photocatalyst can maintain a higher activity

**Table 1**
Photocatalytic performance in laboratory experiments under UV light.

| | $r_i$/mmol $g^{-1}$ $h^{-1}$ | $r_f$/mmol $g^{-1}$ $h^{-1}$ | $TOF_f^a$/ $h^{-1}$ | $C_{mol}(H_2)$/ %[b] | $pH_f^c$ |
|---|---|---|---|---|---|
| $^{h}Pt/TiO_2$ | 267[d] | 51.6[e] | 604 | 95.0 | 3.31 |
| $^{ca}Pt/TiO_2$ | 404[f] | 25.6[g] | 278 | 96.5 | 3.42 |
| $^{ca}Cu/TiO_2$ | 26.0[h] | 10.1[i] | 89 | 78.4 | 3.92 |

Experimental conditions: photocatalyst suspensions (0.5 g $L^{-1}$) in aqueous ethanol (250 mL, 5 mol $L^{-1}$) under UV lamp irradiation (450 W) at initial pH = 7. [a] Calculated based on $H_2$ evolution rate and surface metal co-catalyst atoms. [b] $C_{mol}(H_2)$: Hydrogen molar fraction in the gas produced. [c] $pH_f$: final pH measured at the end of the photocatalytic experiments. Initial gas production rates ($r_i$, average) measured between $t = 0.04$ and 1.50 h (*d*), $t = 0.04$ and 1.00 h (*f*), and $t = 0.17$ and 1.11 h (*h*). Final gas production rates ($r_f$, average) measured between $t = 2.5$ and 24.0 h (*e*), $t = 4.0$ and 24.0 h (*g*), and $t = 6.0$ and 24.0 h (*i*).

for prolonged periods, despite slightly slower initial rates. It should be noted that the gas produced after 24 h is mostly composed of hydrogen (≥95%, Table 1). Based on eventual Pt nanoparticle sizes upon irradiation (see below), TOF values for hydrogen evolution during the latter steady gas production stages are 604 and 278 $h^{-1}$ for $^{h}Pt/TiO_2$ and $^{ca}Pt/TiO_2$, respectively. Minor products including $CH_4$, CO, $CO_2$ and $C_2H_4$ are formed in marginally larger amounts on $^{h}Pt/TiO_2$ (Table S1). Hydrogen concentration increases in both cases at longer times, suggesting that gaseous by-products neither inhibit photoreforming nor impair hydrogen selectivity to any significant extent. Among other possible factors leading to the progressive deceleration of gas production, the accumulation of acetaldehyde as the primary derived intermediate has been postulated as an inhibitor owing to its much lower effectiveness as an electron donor in the process [34]. The expected subsequent degradation into acetic acid [26,34], suggested by the noticeably low final pH of the reaction media (3.3–3.4, Table 1), may result in a similar detrimental effect on activity. This has been more extensively examined by ATR-FTIR spectroscopy, as discussed below.

Copper is less active as a photoreforming co-catalyst than platinum [15]. Accordingly, gas production employing $^{ca}Cu/TiO_2$ is less efficient than in the case of any of the $Pt/TiO_2$ photocatalysts. However, rates do not decrease so drastically upon irradiation for the copper material (Fig. 2b). A faster production of gases is observed during initial stages and a steady rate is achieved for longer irradiation times (26.0 and 10.1 mmol $g^{-1}$ $h^{-1}$, respectively, latter stage TOF = 89 $h^{-1}$, Table 1). The *in-situ* reduction of $Cu^{\delta+}$ species under UV irradiation is expected to readily result in the formation of $Cu^0$ nanoparticles exerting photoreforming activity, as suggested by a clearly apparent colour change of the suspensions from off-white to bright purple [50,68]. Such process is fast as compared to the photocatalytic experiment time, and hence, no induction period is observed. Hydrogen is also the major product in the produced gaseous stream, although in smaller proportions than for the platinum counterparts (Table S1). Significant amounts of carbon products are also produced, as observed for similar photocatalysts, indicating a lower selectivity to $H_2$, especially at initial stages [50]. Among them, CO predominates, especially upon prolonged irradiation, although it does not lead to any serious inhibiting effects. The decreased pH of the $^{ca}Cu/TiO_2$ reaction medium after 24 h (Table 1) also indicates accumulation of acidic products from ethanol photoreforming.

### 3.3. Solar photocatalytic hydrogen production

Photoreforming performance under natural sunlight was tested in a compound parabolic collector reactor under continuously recirculating suspensions of the photocatalysts in water/ethanol media (see Experimental Section). The experiments were conducted in mostly sunny days at LNEG premises (Lisbon, Portugal) during approximately central hours around solar noon. Cumulative gas production was recorded alongside global solar irradiance and temperature (Fig. 3 and Table 2). Irradiance profiles were similar for the three experiments performed (800–1000 W $m^{-2}$), thus making direct comparison between photocatalysts reasonable. All three materials resulted in fairly sustained production rates. Photoreforming activity clearly increased in the following order: $^{ca}Cu/TiO_2$ < $^{ca}Pt/TiO_2$ < $^{h}Pt/TiO_2$, as expected and in accordance with the results obtained from UV laboratory experiments (see above). The composition of the produced gas reveals more selective solar hydrogen production (≥98% $H_2$ and lower amounts of carbon products) than for UV laboratory experiments (Table 2 and S1). Moreover, photocatalytic activities under natural sunlight were lower by a factor of only 5–7 as compared to those under Hg lamp irradiation, despite a 18-fold lower UV irradiance than under Hg lamp light, *i.e.* ≈ 50 (as for standard sunshine conditions) [55] *vs.* ≈ 900 W $m^{-2}$, respectively. Since photocatalysts based on titania operate mainly under irradiation with photons of energy equal to or greater than its bandgap (>3.2 eV, exclusively in the UV region), photonic efficiency is higher in the compound parabolic collector reactor under natural sunlight, a fact which might be due to

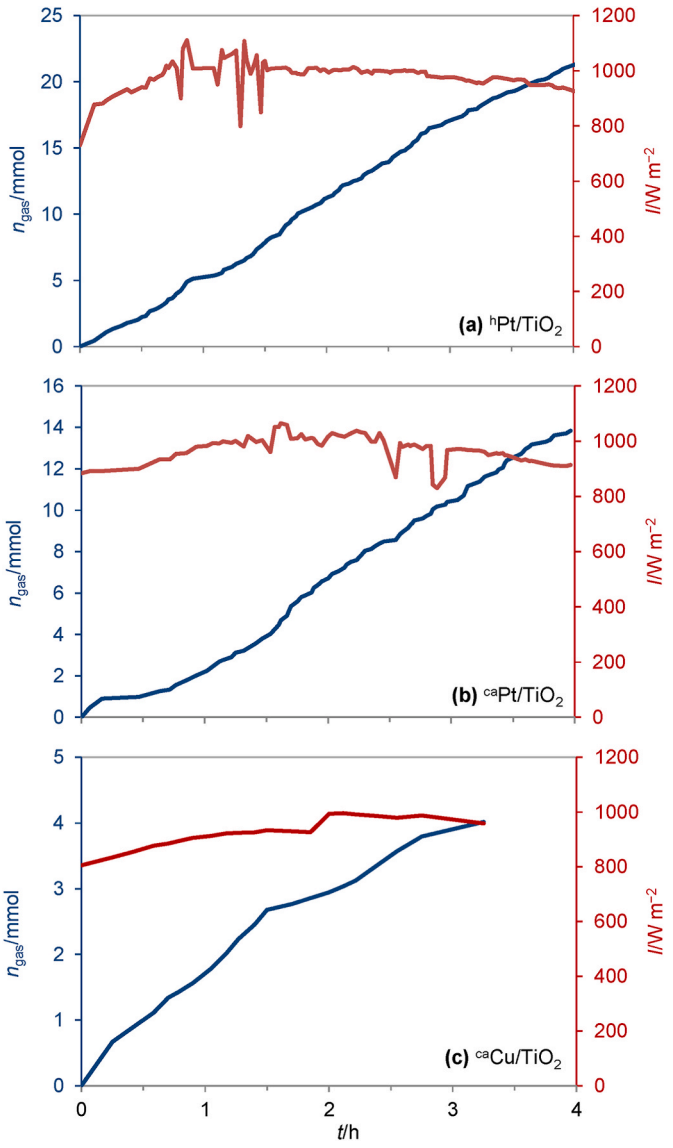


**Fig. 3.** Photocatalytic hydrogen production and measured global irradiance during experiments under natural sunlight performed in a tubular borosilicate glass tubular reactor mounted on a compound parabolic collector from a continually recirculated aqueous ethanol (1.5 L, 5 mol $L^{-1}$) suspensions of the desired photocatalyst (0.5 g $L^{-1}$), under anaerobic conditions (after purging with $N_2$). The cumulative amounts of gas produced ($n_{gas}$) are plotted alongside the recorded global solar irradiance (*I*). [a] Performed on August 8th, 2022, 10:45–14:45, using $^{h}Pt/TiO_2$. [b] Performed on August 10th, 2022, 10:45–14:45, using $^{ca}Pt/TiO_2$. [c] Performed on October 13th, 2021, 10:45–14:00, using $^{ca}Cu/TiO_2$.

reactor geometry and/or to a saturated radiant regime in the experiment using Hg lamp whereby surplus photons are either dispersed or lead to electron-hole recombination [69].

Solar photocatalytic hydrogen production on $^{h}Pt/TiO_2$ maintains a linear trend during the entire experiment duration at a rate near 7.6 mmol $g^{-1}$ $h^{-1}$. The gas production efficiency of the parent $^{ca}Pt/TiO_2$ was lower (5.2 mmol $g^{-1}$ $h^{-1}$). Moreover, a lower rate was observed during the first 2 h than during latter stages (Fig. 3b). This might be related to changes occurring to the atomically dispersed co-catalytic platinum species during irradiation, *i.e.* progressive coalescence and reduction of $Pt^{\delta+}$ into $Pt^0$ nanoparticles, as extensively discussed below. The activity of the copper analogue $^{ca}Cu/TiO_2$ was, by contrast, slightly higher at the beginning of the solar irradiation. Photo-induced *in-situ* reduction of the Cu co-catalyst into metallic species took place after a few minutes of

**Table 2**
Photocatalytic performance in outdoors experiments under natural sunlight.

| | $r^a$/mmol $g^{-1}$ $h^{-1}$ | $I_g^b$/W $m^{-2}$ | $T$(range)$^c$/ °C | $C_{mol}(H_2)$/ % | $pH_f$ |
|---|---|---|---|---|---|
| $^{h}Pt/TiO_2$ | 7.56 | 983 ± 52 | 37–42 | 98.0 | 4.52 |
| $^{ca}Pt/TiO_2$ | 5.18 | 973 ± 50 | 37–42 | 98.3 | 4.88 |
| $^{ca}Cu/TiO_2$ | 1.70 | 925 ± 54 | 38–50 | -$^d$ | 5.13 |

Experimental conditions: photocatalyst suspensions (0.5 g $L^{-1}$) in aqueous ethanol (1.5 L, 5 mol $L^{-1}$) under natural sunlight irradiation collected by a compound parabolic collector after purging with $N_2$. [a] Average gas production rates ($r$) during the entire experiment duration. [b] Average and standard deviation of global irradiance ($I_g$) measured during the entire experiment duration. [c] Temperature outside tubular reactor measured using a thermocouple. [d] Gas composition could not be measured due to insufficient gas volume sampled.

solar irradiation, as indicated by a clear colour change of the suspension into bright purple (Fig. S4). Deactivation phenomena cannot be ruled out in the latter case upon prolonged solar irradiation, but the decrease in activity is not significant during the experiment time frame, and other factors might be at play. The accumulation of ethanol degradation intermediates took place to a lesser extent than during laboratory experiments under more intense UV light, as suggested by lowered pH after natural sunlight irradiation, in agreement with the lower photoreforming rates (Table 2). By analogy to Hg lamp experiments, further acidification and decreased photoreforming rates might be observed for longer exposure to solar UV photons too. In summary, the results obtained under natural sunlight using our compound parabolic collector reactor prove that steady gas production by photoreforming is feasible and scalable. Most recent related literature data, as comparatively collected in Table S2, have been recorded in small-scale laboratory setups, and although some productivities (in mmol $g^{-1}$ $h^{-1}$) are remarkable [49,70–73], their absolute time yields are generally lower than those in our experiments. Conversely, the scarce upscaled pilot-plant literature examples show promising productivities commensurate with the ones reported herein (around or above 10 mmol $h^{-1}$) [74–77].

### 3.4. Chemical evolution of Pt or Cu co-catalysts under irradiation

The electronic spectra of the photocatalysts before and after use have been recorded to gain insight into the evolution of their optical and physicochemical properties under irradiation. The corresponding DRUV-vis-NIR spectra are displayed in Fig. 4a–c. The absorption edge at *ca.* 400 nm due to bandgap absorption by $TiO_2$ is noticeable for all samples. Conversely, changes in the absorption profiles in the visible and near infrared regions upon irradiation are observed. Such changes took place to different degrees depending on the photocatalyst, reflecting distinct evolution of the co-catalysts. In the case of $^{h}Pt/TiO_2$, the continuum of absorbance extending throughout the vis-NIR region is attributed to a combination of d–d transitions [78] and to weak and broad signals due to photonic absorption by metallic Pt nanoparticles [79]. These vis-NIR features are barely affected by natural sunlight irradiation, although some changes are apparent after UV photocatalysis. Specifically, a slight but noticeable and steady increase of the visible absorption fingerprint intensity after UV irradiation suggests Pt reduction, probably of thin passivation layers formed under ambient air after preparation.

The calcined $^{ca}Pt/TiO_2$ shows a featureless absorption profile in the visible and into the NIR regions, in accordance with the pale yellowish colour of the solid and with the expected predominance of oxidised platinum species [80]. During and after photocatalysis, either solar or UV, the suspensions rapidly turned grey. This is reflected in the spectra, exhibiting increased absorbance (lower reflectance) in the vis-NIR spectral range (Fig. 4b), eventually resembling those for the activated counterpart ($^{h}Pt/TiO_2$, see above). Therefore, it can be inferred that oxidised platinum co-catalyst species underwent light-induced reduction into $Pt^0$, as expected; XPS results presented below confirm this phenomenon.

The vis-NIR region of the spectra of fresh $^{ca}Cu/TiO_2$ is consistent with the presence of $Cu^{II}$, *i.e.* exhibiting a broad signal between 700 and 1100 nm [50,81], whereas some minor contribution from $Cu^0$ or $Cu^I$ cannot be ruled out (Fig. 4c). After photocatalysis, the bands associated with CuO are greatly diminished. Conversely, shoulders are observed below 600 nm, probably due to partial reduction into $Cu_2O$ and/or $Cu^0$ [81]. The transient formation of $Cu^0$ nanoparticles is strongly suggested by the intense purple colour of the suspensions under either solar or UV irradiation (Fig. S4), although rapid re-oxidation takes place in the dark or under lower irradiance, as suggested by the discolouration observed in such events. Such *in-situ* re-oxidation events have been related to partial loss of copper during solid recovery in the dark [43,44,81]. This partly accounts for the overall lower absorbance after photocatalysis, as observed in the spectra, and is further confirmed below by XPS and EDS results. Future *in-situ* DURV-vis-NIR studies are being considered to more precisely track the evolution of copper species in $Cu/TiO_2$ materials during photocatalytic operation.

The optical bandgaps of the photocatalysts have been determined by converting the reflectance data into Tauc plots (Fig. S5). All fresh materials exhibit bandgap energies in accordance with the expected absorption edge of $TiO_2$ (*ca.* 3.2 eV), whilst small differences may be due to slight distortion caused by contribution of d-d transitions from metal co-catalysts. Bandgaps are remarkably similar (*ca.* 3.11 ± 0.5 eV) for all photocatalysts after irradiation, and hence, no clear correlation between activity and optical absorption can be inferred.

The oxidation states of Pt and Cu co-catalysts were determined by XPS to complement the results obtained by DRUV-vis-NIR spectroscopy. High-resolution Pt 4f and Cu 2p spectra for the fresh photocatalysts were taken to elucidate initial oxidation states and their evolution during photocatalysis was studied by comparison with spectra for the used materials (Fig. 4d–f). Furthermore, the corresponding Ti 2p, O 1s and C 1s spectra are shown in Figs. S6–S8. Only one Pt $4f_{7/2}$ component centred at around 71.0 eV (Fig. 4d and Table S3), consistent with $Pt^0$, was identified for the reduced platinum photocatalyst, *i.e.* $^{h}Pt/TiO_2$ [62,82]. The spectra recorded after either UV or natural solar irradiation were essentially unchanged, confirming that the pre-reduced platinum co-catalyst species in $^{h}Pt/TiO_2$ were stable from a chemical perspective. The presence of any surface-oxidised Pt domains is either negligible or below the detection limit of the XPS technique.

As anticipated based on electronic spectroscopy above, the as-calcined material contained a mixture of platinum species in different oxidation states. Its Pt $4f_{7/2}$ signal can be deconvoluted into three components centred at 71.1, 72.0 and 73.8 eV (Fig. 4e and Table S4), attributed to $Pt^0$, $Pt^{II}$ and $Pt^{IV}$, respectively [62,64]. Their relative atomic abundances are 8, 32 and 60%, respectively, indicating the expected predominance of oxidised platinum species, and the formation of a small fraction of metallic platinum, most likely by self-reduction during calcination. Upon irradiation, both under UV and solar light, all oxidised platinum was essentially reduced to $Pt^0$, as indicated by the prevalence of only one kind of Pt $4f_{7/2}$ signals at 70.5–70.7 eV (Fig. 4e), slightly shifted to negative binding energies relative to the expected metallic platinum signal. Such low energy signals suggest enhanced electron transfer from the $TiO_2$ support to the nascent Pt nanoparticles in $^{ca}Pt/TiO_2$ upon irradiation, as opposed to the standard Pt electron density revealed by the expected $Pt^0$ signal at 71.0 eV for $^{h}Pt/TiO_2$. A possible explanation for this observation may lie in the particular growth and aggregation of $Pt^0$ nanoparticles into clustered domains, as described in the section below about morphological evolution. Overall, reduction into metallic nanoparticles is clear, and these results are in agreement with those obtained by DRUV-vis-NIR (see above and Fig. 4b), which also indicated *in-situ* photo-reduction of $Pt^{\delta+}$ into $Pt^0$.

The case of copper is greatly dependent on its redox lability both under irradiation and in the dark. The XPS spectrum of as-calcined $^{ca}Cu/$

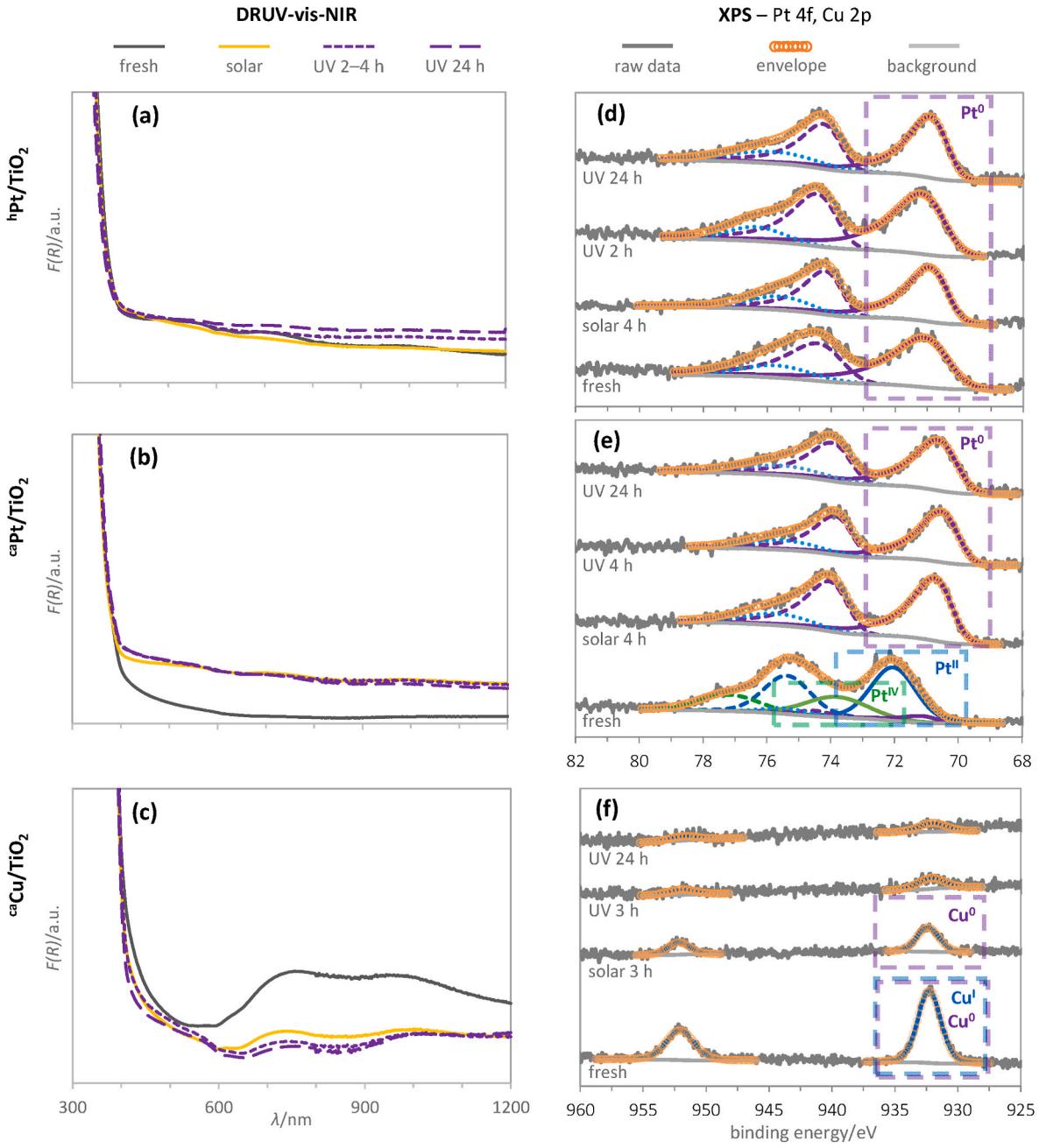


**Fig. 4.** Evolution of the optical absorption properties of the studied photocatalysts based on DRUV-vis-NIR (a–c) and on XPS (d–f) spectra. Samples were analysed as freshly prepared, or after use under natural sunlight or UV Hg lamp irradiation for short (2–4 h) or long (24 h) times. Components detected by XPS for each metallic oxidation state are indicated in boxes; solid traces for the Pt $4f_{7/2}$ and Cu $2p_{3/2}$ region; dashed traces correspond to analogous signals in the Pt $4f_{5/2}$ and Cu $2p_{1/2}$ region; dotted blue traces correspond to Ti 3s plasmon loss signals overlapping with those for Pt $4f_{5/2}$ electrons. (For interpretation of the references to colour in this figure legend, the reader is referred to the Web version of this article.)

$TiO_2$ reveals the presence of either $Cu^I$ or $Cu^0$ species (Fig. 4f); a mixture of both was probably present, based on the Cu LMM signal (Fig. S9). No sign of $Cu^{II}$ could be detected by XPS, in contrast to what was observed in electronic spectra described above. This could be due to higher sensitivity of DRUV-vis-NIR, and/or to reduction under X-rays, whereas the possibility of CuO formed deep below surface is ruled out given the high (atomic) dispersion of copper species (see discussion on dispersion and morphological evolution studied by HRTEM and STEM below). After irradiation under natural sunlight, signal intensity decreases but shows little or no shifting in binding energy. In this case, the signal in the Cu LMM region suggests that copper was reduced to its metallic state (Fig. S9). In agreement with optical absorption spectroscopy, the surface concentration of copper was significantly decreased due to re-oxidation and leaching of copper upon ceasing irradiation [42–44,81]. The amounts of copper on the surface were lower after UV irradiation than after natural sunlight experiments (Cu/Ti atomic ratios: 0.2–0.4% *vs.* 1.1%, respectively, Table S5).

### 3.5. *Morphological evolution of Pt or Cu co-catalysts under irradiation*

Post-photocatalysis morphological characterisation was performed in this study to assess the evolution of co-catalyst domains under irradiation, either high-intensity UV or natural sunlight. In the former case, this was done after different lengths of irradiation times to track both

short- and long-term photonic exposure effects. Investigations of this kind are surprisingly scarce in the literature with notable exceptions [31,38,40,41], especially for prolonged irradiation times and relatively high Pt loadings, as studied in this work (1% ratio on a mass basis). Once the UV effect on co-catalyst evolution was understood, analogous characterisation after natural solar irradiation was undertaken. One question to address is whether the evolution of the co-catalyst follows the same paths but at different paces in either case according to the relative proportion of UV photons in solar irradiation, and hence, to the total UV irradiance. In our experiments, UV-A + UV-B irradiances were *ca.* 3.2 $10^2$ + 5.7 $10^2$ W $m^{-2}$ and 52 + 0.1 W $m^{-2}$ under Hg lamp irradiation or natural sunlight, respectively, as measured by employing a pyranometer and appropriate sensors (see Experimental Section).

The reduced $^{h}Pt/TiO_2$ photocatalyst, containing Pt nanoparticles mainly in the 1–3 nm diameter range when fresh (Fig. 5b), retained its morphology and co-catalyst distribution pattern throughout different experimental irradiation conditions, based on multiple measurements from STEM-HAADF images. The Pt nanoparticle size distribution remained essentially unchanged after either UV or solar irradiation for any length of time within experimental error (1.8 ± 0.6 nm, Fig. 6 and Table S6). Qualitative comparison of STEM images confirms the invariability of Pt co-catalyst distribution and morphology; neither clustering nor disaggregation of nanoparticles took place during photocatalysis (Fig. S10). Based on these observations, the integrity of the Pt nanoparticles formed upon thermal activation under $H_2$ atmosphere was retained during photocatalysis under a range of different experimental conditions. Most likely, platinum remains completely reduced, and moreover, any possible minor $PtO_x$ passivation layers formed in contact with ambient air tend to become reduced to metallic form, under the irradiated anaerobic conditions employed. Therefore, little or no redissolution of cationic platinum, which might lead to migration and re-reduction and deposition on existing $Pt^0$, is expected. In other words, ripening mechanisms can be largely ruled out. Therefore, the slight activity decline observed after several hours of photocatalysis, especially in the case of experiments under UV (Fig. 2a), cannot be ascribed to photocatalyst (or co-catalyst) evolution, but rather to accumulation of ethanol degradation intermediates, as postulated below.

The case of the calcined $^{ca}Pt/TiO_2$ photocatalyst is markedly different regarding co-catalyst morphological evolution under irradiation. Noticeable growth of Pt nanoparticles is obvious based on HRTEM and STEM images recorded after any of the photocatalytic experiments, in contrast to the fine dispersion of platinum in the fresh material (Fig. 5c,d and Figure S11). The evolution of Pt co-catalyst from atomically dispersed and sub-nanoparticles takes place into slightly smaller nanoparticles after solar irradiation than under UV, as observed by HRTEM (Fig. 5c and d, respectively). Quantitative confirmation of the slower Pt coalescence under natural sunlight as compared to UV was drawn by statistical processing of Pt nanoparticle diameter measurements from STEM micrographs (Fig. 6 and Figure S11). After 4 h under UV light, a large proportion of Pt had grown into nanoparticles of diameters within a 1–2 nm range, although a significant number of sub-nanoparticles remained (see Fig. 5d, Figure S11 and Table S7). This can be described as a bimodal particle size distribution whereby some atomically dispersed Pt starts diffusing and depositing by reduction into

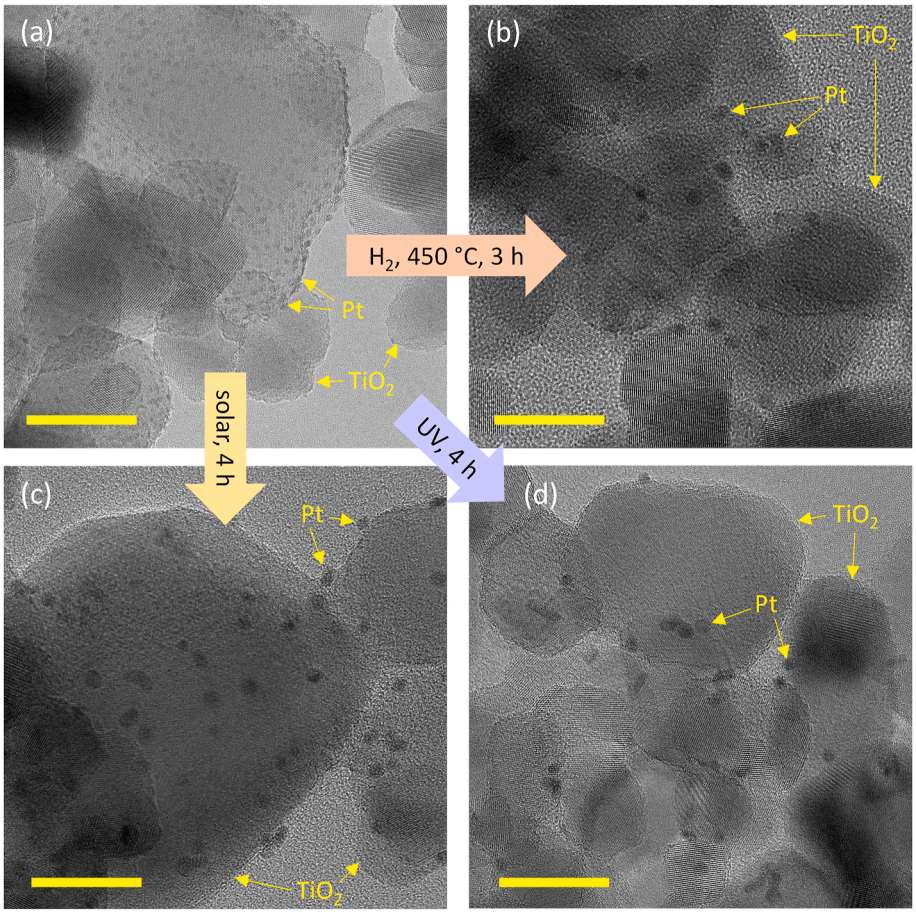


**Fig. 5.** Representative HRTEM micrographs illustrate the evolution of atomically dispersed platinum and sub-nanoparticles in $^{ca}Pt/TiO_2$ (a), after thermal reduction under hydrogen leading to $^{h}Pt/TiO_2$ (b), and post-photocatalysis under either natural sunlight (c) or UV irradiation (d). Examples of Pt nanoparticles and $TiO_2$ support are pinpointed with yellow arrows for clarity. Scale bars: 20 nm. (For interpretation of the references to colour in this figure legend, the reader is referred to the Web version of this article.)

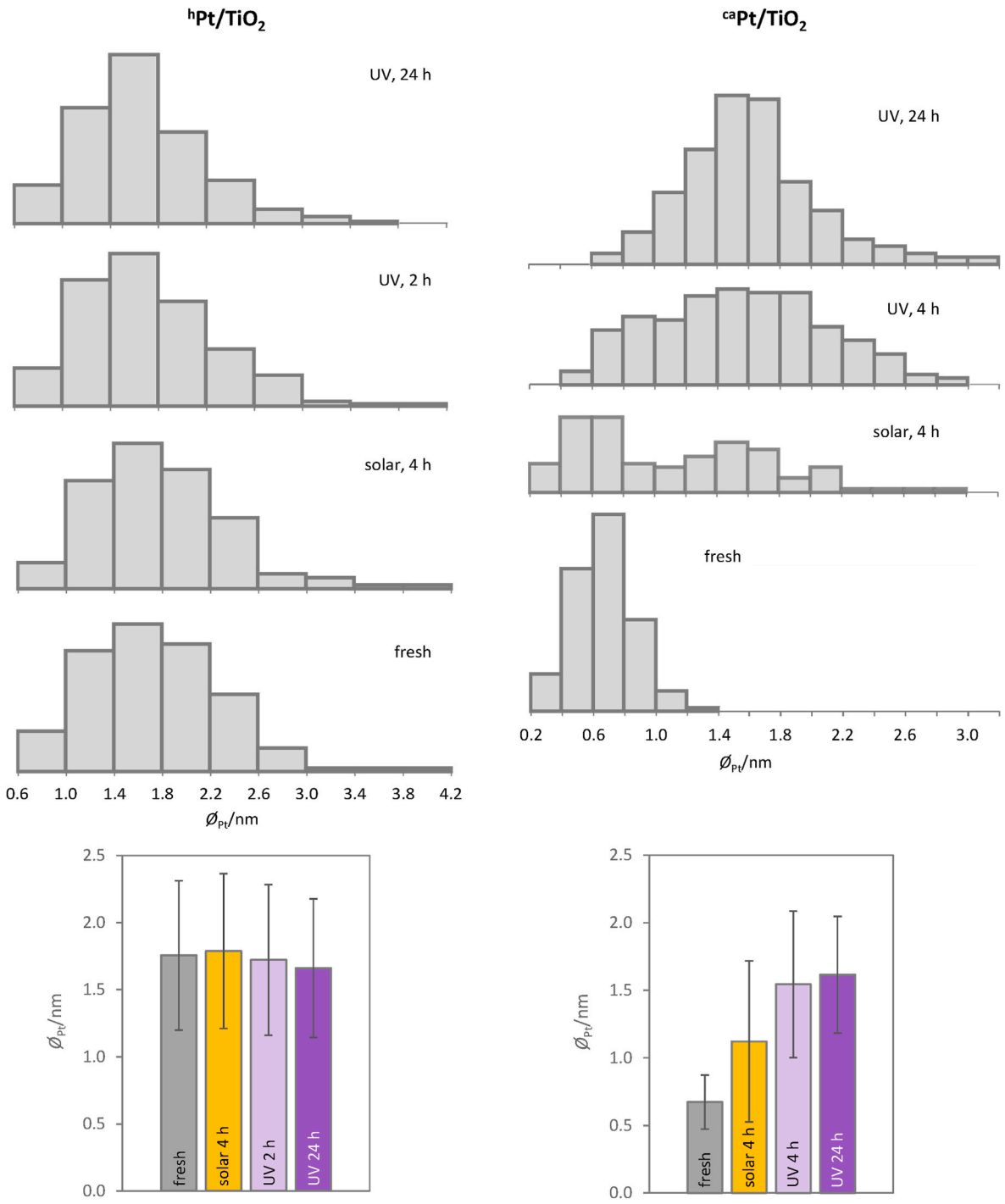


**Fig. 6.** Evolution of platinum particle sizes in reductively activated $^{h}Pt/TiO_2$ and as-calcined $^{ca}Pt/TiO_2$ photocatalysts, after use under either natural sunlight or UV Hg lamp irradiation for different lengths of time, as compared to the fresh solids. Particle sizes were measured as projected diameters from STEM-HAADF images as indicated in the Supplementary Material. Vertical axes of the histograms are not normalised to provide a relatively realistic comparison on number of particles identified per diameter range.

existing $Pt^0$ particles of different sizes. After solar irradiation, whereby the process is slower, the bimodal distribution of sizes is even clearer, thus confirming the proposed ripening mechanism on two size levels (see histograms in Fig. 6, right). Prolonged UV irradiation resulted in a further coalescence of Pt into nanoparticles and minor amount of sub-nanometric domains (average particle sizes: 1.6 ± 0.4 nm, Fig. 6 and Table S7). Interestingly, final Pt particle sizes are almost identical to those of thermally reduced $^{h}Pt/TiO_2$ before and after UV photocatalysts. One plausible reason for this phenomenon is the tendency of metallic Pt nanoparticles to evolve to their most thermodynamically favoured size distribution (1–2 nm), owing to surface free energy minimisation [28]. Recent findings suggest that hydrogen adsorption on single atoms weaken their bonding to the support, in turn enabling detachment and migration mechanisms that eventually result in Pt sintering [83].

Photocatalytic activity differences between $^{h}Pt/TiO_2$ and $^{ca}Pt/TiO_2$, especially at long UV irradiation times (Fig. 2a and $r_f$ in Table 1), cannot be rationalised based on Pt particle size effects, since they eventually become similar (1.7 ± 0.5 and 1.6 ± 0.4 nm, respectively, Table S6 and

S7). This might be partly understood by closely looking at minor morphological differences of samples after 24 h irradiation under Hg lamp light, based on STEM-HAADF images (Fig. S10 and S11). Despite essentially identical sizes, Pt nanoparticles in $^{h}Pt/TiO_2$ remained well separated, whereas most of those in $^{ca}Pt/TiO_2$ grew tightly contacting each other, often as pseudo-clusters or caterpillar-like pseudo-lines of nanoparticles. Such proximity and contacts might reduce the amount of available active sites for $H_2$ generation. Conversely, the much faster hydrogen production activity of $^{ca}Pt/TiO_2$ at shorter UV irradiation times (≈400 mmol $g^{-1}$ $h^{-1}$ at < 2 h, Fig. 2a and $r_i$ in Table 1) could be due to the rapid transient formation and growth of small nascent $Pt^0$ nanoparticles of sizes around 1 nm. Both experimental [31,84] and theoretical [85] reports agree on a maximum photocatalytic $H_2$ production activity for such small nanometric size range. Subsequent growth into the more thermodynamically favourable, albeit partly aggregated, larger nanoparticles would result in the observed activity decline. Other reports on $TiO_2$ layers or nanosheets with a majority of (001) facets exposed propose that only Pt single atoms are active for hydrogen evolution [39,40,86]. This is unlikely to be the case here for $^{ca}Pt/TiO_2$ since low activity is observed under natural sunlight up to 1.5 h (Fig. 3b), in spite of the higher proportion of atomically dispersed Pt during initial stages, as compared to the faster $H_2$ evolution rate during latter stages. This suggests that the growth of $Pt^0$ nanoparticles beyond a critical size of around 1 nm, which takes place at much slower pace under natural solar —hence lower UV-intensity— light (Fig. 6, right), determines an induction period for active site formation. In other words, single atoms would prevail during the initial stage of lower activity, whereas the nascent $Pt^0$ nanoparticles after the induction period would promote $H_2$ evolution (0–1.5 h and 1.5–4.0 h, respectively, in Fig. 3b). Conversely, the induction process might take place too quickly under strong UV irradiation to be distinguished (Fig. 2a).

The evolution of copper co-catalysts on titania differs greatly as compared to that for platinum counterparts. The first obvious difference is the almost complete absence of copper domain growth or aggregation into nanoparticles (Fig. S12). By contrast, the high dispersion of copper in fresh $^{ca}Cu/TiO_2$ was maintained or even enhanced, and importantly, the number of particles found was noticeably lower after photocatalysis (Fig. 7 and Table S8). This might be due to atomic dispersion of the copper co-catalyst or to leaching caused by photocorrosion. Elemental analyses performed by SEM-EDS indicate a drastic decrease in Cu loadings in the used photocatalysts (from *ca.* 1.0% to <0.2%, Fig. S13), suggesting that the latter hypothesis is more plausible. Conversely, no Pt losses are observed for neither $^{h}Pt/TiO_2$ nor $^{ca}Pt/TiO_2$. The photocatalytic activity of $^{ca}Cu/TiO_2$ under both UV and solar irradiations is steady and remarkably high despite the loss of co-catalyst after reaction (see above). A reasonable explanation for this apparent contradiction lies in the particular behaviour of copper, which can be cyclically oxidised and reduced under operation in $TiO_2$ photocatalysts [42,51,68,81]. Kondarides and co-workers demonstrated this by analysing the results of extensive glycerol photoreforming experiments [50]. Under irradiation, copper is readily reduced into metallic nanoparticles deposited on $TiO_2$, whilst the process can be rapidly reversed when irradiation ceases, as demonstrated by Fornasiero and co-workers [43,44]. In our own outdoors solar experiments, such *in-situ* photoreduction of copper was apparent, as suggested by the colour change of the suspensions from off-white to purple under sunlight (Fig. S4). A similar phenomenon took place under UV irradiation. The actual role of copper as a co-catalyst has been proven by comparing gas productivity of $^{ca}Pt/TiO_2$ with that of the bare support ($TiO_2$ P 25) under UV light (Fig. S14). Although gas is produced by the latter initially, activity slows down and nearly halts completely after 10 min. By contrast, gas production is significantly steadier and faster upon irradiation for several hours, thus confirming that copper co-catalyst species promote photoreforming, despite the leaching phenomena that takes place after light is switched off.

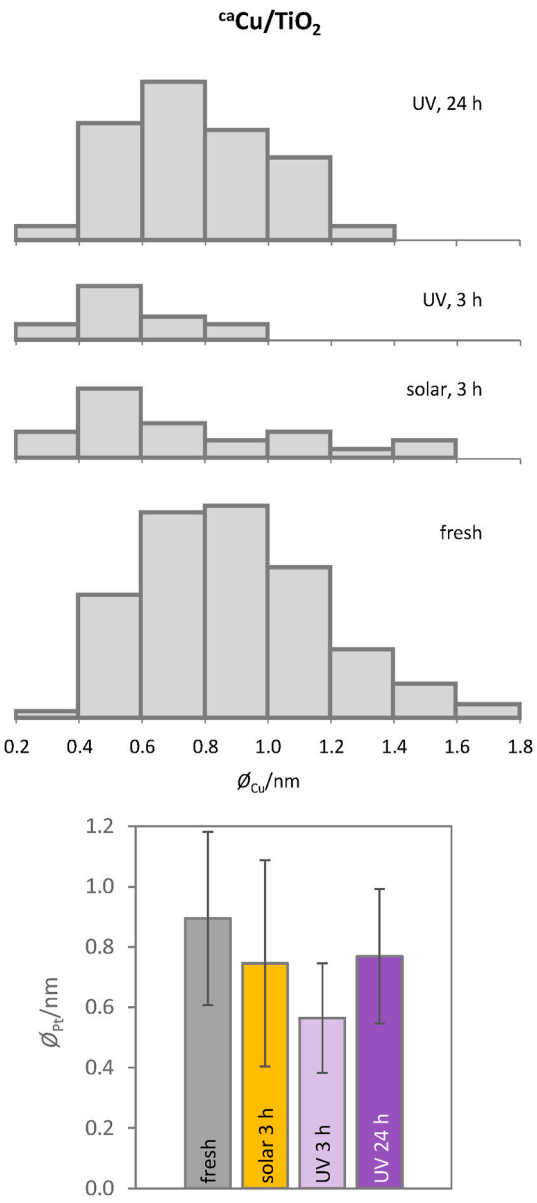


**Fig. 7.** Evolution of copper particle sizes in calcined $^{ca}Cu/TiO_2$, after use under either natural sunlight or UV Hg lamp irradiation at different times, as compared to the fresh solid. Particle sizes were measured as projected diameters from STEM-HAADF images as indicated in the Supplementary Material. Vertical axes are not normalised to provide a relatively realistic comparison on number of particles identified per diameter range.

### 3.6. Detection of adsorbed intermediates and their inhibitory effects

In addition to the oxidation state and morphological evolution of the metal co-catalyst, the originally clean and accessible surface of the photocatalysts might become progressively covered with photoreforming intermediates, possibly blocking active sites, and hence, limiting their availability for further adsorption and conversion of ethanol [15]. The primary ethanol photoreforming intermediate is acetaldehyde, as the product of rapid oxidative dehydrogenation [26,34,87–90], whereas subsequent oxidation to other oxygenated organic intermediates, chiefly acetic acid (or acetate), formic acid (or formate) and formaldehyde, can take place [26,34,87,89–91]. In order to assess the possible accumulation of adsorbed intermediates, ATR-FTIR spectra of the solids before and after irradiation were recorded (Fig. 8 and Fig. S14). The spectra of the fresh photocatalysts are featureless, with

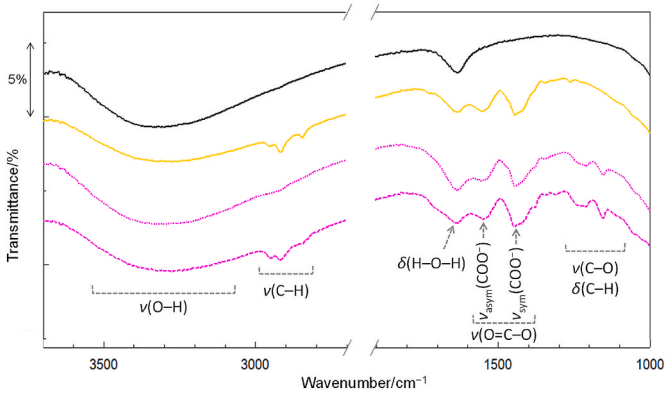


**Fig. 8.** ATR-FTIR spectra of $^{h}Pt/TiO_2$ as freshly prepared (black trace), or after use under natural sunlight (yellow trace) or UV Hg lamp irradiation for short (2–4 h, dotted purple trace) or long (24 h, dashed purple trace) times. Assignment of signals to main functional groups of adsorbed species are shown. (For interpretation of the references to colour in this figure legend, the reader is referred to the Web version of this article.)

the exception of broad bands between 3700 and 2800 $cm^{-1}$ and sharper peaks at *ca.* 1640 $cm^{-1}$ due to O–H stretching vibrations and H–O–H bending of adsorbed water, respectively. A set of additional signals is observed after any of the photocatalytic experiments, indicating the presence of new surface absorbed species. It is striking and worthwhile noting that adsorbed intermediates remain bound to the photocatalyst surfaces even after solid separation, washing and drying at 60 °C.

Several peaks in the 2800–3000 $cm^{-1}$ regions, indicative of C–H stretching [92], are observed for almost all samples. Moreover, two signals at *ca.* 1560 and 1440 $cm^{-1}$ consistent with the asymmetric and symmetric stretching modes of carboxylate moieties [93–95], respectively, are invariably and clearly present in all spectra. These bands might include overlapped contribution of adsorbed carbonate/bicarbonate species [96,97], although they are expected to be minor as a consequence of protonation and ensuing $CO_2$ release at the pH achieved during irradiations, lower than the p$K_a$ of carbonic acid (6.35). For some samples, especially those recovered after UV photocatalysis, bands in the 1300–1100 $cm^{-1}$ region, that might be attributed to C–O stretching and/or C–H bending absorptions [92,98], are also observed. The strong carboxylate bands suggest that aliphatic carboxylate intermediates, most likely acetate species, are produced during the photoreforming of ethanol and accumulate on the surface of the photocatalysts. The presence of two bands at around 1220 and 1360 $cm^{-1}$ for $^{h}Pt/TiO_2$ and $^{ca}Pt/TiO_2$ after UV irradiation (Fig. 8 and Fig. S14) could be due to overoxidation into more oxygenated species such as glyoxylate [99], or into lower oxygenates such as formaldehyde or formate after C–C cleavage [92,98]. Conversely, these signals are absent for samples after solar experiments (orange traces, Fig. 8 and Fig. S14), possibly owing to slower oxidation events and/or to the lower oxidative power of the less UV-rich sunlight radiation.

Spectra for $^{ca}Cu/TiO_2$ photocatalysts are qualitatively similar to those for the platinum counterparts (Fig. S14), meaning that ethanol degradation pathways are essentially parallel, although adsorbate signals are significantly less intense in the case of the copper co-catalyst. This is consistent with the slower photoreforming on $^{ca}Cu/TiO_2$, yet interestingly, the less extensive surface coverage with intermediate oxygenated by-products leaves a larger fraction of available active sites for ethanol adsorption and oxidation. We postulate that this is the reason why deactivation/inhibition events on $^{ca}Cu/TiO_2$ are less severe than on $Pt/TiO_2$ materials, especially under UV irradiation (see Fig. 2 and Table 1). In other words, the remarkably fast photoreforming with platinum as a co-catalyst becomes limited by blocking of active sites, most likely oxidative active sites on titania surfaces, due to accumulation of adsorbed ethanol oxidation products after a critical irradiation time (sudden slope changes after 2 h in Fig. 2a). This phenomenon is most obvious in the case of $^{h}Pt/TiO_2$: Since little or no changes in Pt nanoparticle size, shape or distribution are apparent, reaction rate deceleration cannot be ascribed to any morphological evolution of the photocatalyst, and hence, build-up of adsorbed carboxylates or aldehydes with slower oxidative degradation kinetics is the most likely cause for the latter slower photoreforming stages [33,34,100].

As inferred from these ATR-FTIR results, the extremely fast hydrogen production on $Pt/TiO_2$ photocatalysts during initial stages of UV irradiation leads to the progressive surface accumulation of adsorbed oxygenated photoreforming intermediates. Further oxidation of such intermediates become rate-limiting at longer times, slowing down gas production. By contrast, the (relatively) slower initial photoreforming on $Pt/TiO_2$ under solar light, or on $Cu/TiO_2$ under either UV or solar irradiations, continues at similar, only marginally decreased rates since the accumulation of adsorbed intermediates takes place to a lower extent. Therefore, their inhibitory effects are much less detrimental on reaction rates for the initially slower systems.

## 4. Conclusions

The metallic co-catalyst species and domains in metal/titania photocatalysts, namely $Pt/TiO_2$ or $Cu/TiO_2$, behave dynamically during photoreforming operation under either UV or natural sunlight irradiations. This has been herein proven for $^{ca}Pt/TiO_2$, prepared by impregnation-calcination on commercial P-25 titania, whereby platinum is mostly atomically dispersed in the form of $Pt^{\delta+}$ single atoms or clusters, with maximum domain diameters below 1 nm. After several hours of irradiation (>2 h under UV, longer under sunlight), platinum single atoms, clusters and sub-nanoparticles evolve into $Pt^0$ nanoparticles (1–2 nm), a process most likely driven by hydrogen adsorption weakening Pt-support interaction, and ultimately, surface energy minimisation. Interestingly, no significant morphological evolution takes place for a material containing pre-formed stabilised $Pt^0$ nanoparticles of similar sizes, formed by thermal pre-reduction under $H_2$ ($^{h}Pt/TiO_2$). Hydrogen production rates from aqueous ethanol under UV light underwent a sudden decrease for both calcined and pre-reduced platinum/titania photocatalysts that cannot be ascribed to the evolution of the Pt co-catalyst sizes or morphologies. Notwithstanding, activity remained remarkably high for up to 24 h (>25 and >50 mmol $g^{-1}$ $h^{-1}$ for $^{ca}Pt/TiO_2$ or $^{h}Pt/TiO_2$, respectively), indicating robust and sustained performance in the long term. Dynamic redox behaviour of copper co-catalysts resulted in reduction into $Cu^0$ sub-nanoparticles but showing no sign of aggregation, both under UV and sunlight irradiations. Similarly to platinum, sustained photoreforming activity was observed for $^{ca}Cu/TiO_2$ for long UV irradiations after a slightly faster initial stage.

The ultimate goal of this work was to assess photocatalytic effectiveness and robustness in solar reactors. In contrast to UV irradiations, hydrogen evolution under natural sunlight maintained an essentially linear trend for all materials from the beginning and throughout several hours. This proves that rearrangement of co-catalyst domains, including the agglomeration of atomically dispersed Pt into reduced metallic nanoparticles, does not result in significant deactivation. By contrast, infrared spectroscopy suggests that the rate declines recorded under UV irradiation are most likely due to the accumulation of ethanol oxidation intermediates, especially adsorbed acetate. In consequence, active sites would become progressively blocked by the slower, rate-limiting, further oxidation of such adsorbates. The effect severely affects photocatalysis under strong UV light, whilst it is almost irrelevant under solar experiments running under lower UV photonic flux, which, hence, proceed at a steady pace. In consequence, hydrogen production by solar photoreforming in compound parabolic collectors is effective and sustained at remarkably high rates, *i.e.* 7.6 and 1.7 mmol $g^{-1}$ $h^{-1}$ for $Pt/TiO_2$ or $Cu/TiO_2$, respectively.

## CRediT authorship contribution statement

**Anabela Capelo:** Writing – original draft, Methodology, Investigation, Formal analysis, Data curation. **Domenico Fattoruso:** Methodology, Investigation, Formal analysis. **Laura Carolina Valencia-Valero:** Methodology, Investigation. **M. Alexandra Esteves:** Writing – review & editing, Validation, Supervision, Resources, Project administration, Methodology, Investigation, Formal analysis, Data curation, Conceptualization. **Carmen M. Rangel:** Writing – review & editing, Supervision, Resources, Project administration, Investigation, Funding acquisition, Conceptualization. **Alberto Puga:** Writing – review & editing, Writing – original draft, Validation, Supervision, Project administration, Methodology, Investigation, Funding acquisition, Formal analysis, Data curation, Conceptualization.

## Declaration of competing interest

The authors declare the following financial interests/personal relationships which may be considered as potential competing interests: Alberto Puga reports financial support was provided by European Union. If there are other authors, they declare that they have no known competing financial interests or personal relationships that could have appeared to influence the work reported in this paper.

## Acknowledgments

This work was funded by European Union's Horizon 2020 research and innovation programme under grant agreement Nº 823802 through a mobility action (SURPF2001310055) within the Access to Solar Facilities for the European Research Area, SFERA III, programme. A.P., L.C. V.-V. are grateful to the Spanish Research State Agency (Agencia Estatal de Investigación, MICIU/AEI/10.13039/501100011033) for research grants PID2020-116322RB-C32 and TED2021-129496B–I00, the latter with funds from NextGenerationEU. Also acknowledged is the HYLANTIC project EAPA_204/2016, co-financed by the European Regional Development Fund, INTERREG ATLANTIC programme. L.C.V.-V. thanks *Universitat Rovira i Virgili* for a pre-doctoral contract (2021PMF-PIPF-15) within its *Marti i Franquès* programme. D.F. thanks the European Generation Foundation for an EU4EU Erasmus+ Traineeship. The TEM instrument was partially funded by the operative program *FEDER Catalunya* 2014–2020 (IU16-015844). The XPS instrument was partially funded by the Spanish Research State Agency (EQC2021-007785-P). Dr. S. Plana and Dr. D. Ruano are gratefully acknowledged for useful discussions on TEM and XPS results, respectively.

## Appendix A. Supplementary data

Supplementary data to this article can be found online at https://doi.org/10.1016/j.ijhydene.2025.01.203.

## References

[1] Balzani V, Armaroli N. Energy for a sustainable world: from the oil age to a sun-powered future. Wiley; 2010.
[2] Armaroli N, Balzani V. The hydrogen issue. ChemSusChem 2011;4(1):21–36.
[3] Gielen D, Taibi E, Miranda R. Hydrogen: a renewable energy perspective. International Renewable Energy Agency (IRENA); 2019.
[4] Global Hydrogen Review 2023. International Energy Agency: Paris, 2023; Vol. Licence: CC BY 4.0.
[5] Navarro RM, Peña MA, Fierro JLG. Hydrogen production reactions from carbon feedstocks: fossils fuels and biomass. Chem Rev 2007;107(10):3952–91.
[6] Kumar R, Singh R, Dutta S. Review and outlook of hydrogen production through catalytic processes. Energy Fuels 2024;38:2601–29.
[7] Alonso DM, Bond JQ, Dumesic JA. Catalytic conversion of biomass to biofuels. Green Chem 2010;12(9):1493–513.
[8] Huber GW, Dumesic JA. An overview of aqueous-phase catalytic processes for production of hydrogen and alkanes in a biorefinery. Catal Today 2006;111(1–2):119–32.
[9] Puga A. Photocatalytic hydrogen production for sustainable energy. Wiley; 2023.
[10] Wang Q, Domen K. Particulate photocatalysts for light-driven water splitting: mechanisms, challenges, and design strategies. Chem Rev 2020;120(2):919–85.
[11] Chen S, Takata T, Domen K. Particulate photocatalysts for overall water splitting. Nat Rev Mater 2017;2(10):17050.
[12] Kudo A, Miseki Y. Heterogeneous photocatalyst materials for water splitting. Chem Soc Rev 2009;38:253–78.
[13] Bhattacharjee S, Linley S, Reisner E. Solar reforming as an emerging technology for circular chemical industries. Nat Rev Chem 2024;8(2):87–105.
[14] Granone LI, Sieland F, Zheng N, Dillert R, Bahnemann DW. Photocatalytic conversion of biomass into valuable products: a meaningful approach? Green Chem 2018;20(6):1169–92.
[15] Puga AV. Photocatalytic production of hydrogen from biomass-derived feedstocks. Coord Chem Rev 2016;315:1–66.
[16] Davis KA, Yoo S, Shuler EW, Sherman BD, Lee S, Leem G. Photocatalytic hydrogen evolution from biomass conversion. Nano Convergence 2021;8(1):6.
[17] Luo H, Barrio J, Sunny N, Li A, Steier L, Shah N, Stephens IEL, Titirici M-M. Progress and perspectives in photo- and electrochemical-oxidation of biomass for sustainable chemicals and hydrogen production. Adv Energy Mater 2021;11(43):2101180.
[18] Christoforidis KC, Fornasiero P. Photocatalytic hydrogen production: a rift into the future energy supply. ChemCatChem 2017;9(9):1523–44.
[19] Jeon TH, Koo MS, Kim H, Choi W. Dual-functional photocatalytic and photoelectrocatalytic systems for energy- and resource-recovering water treatment. ACS Catal 2018;8(12):11542–63.
[20] Rioja-Cabanillas A, Valdesueiro D, Fernández-Ibáñez P, Byrne JA. Hydrogen from wastewater by photocatalytic and photoelectrochemical treatment. J Phys: Energy 2020;3(1):012006.
[21] Uekert T, Pichler CM, Schubert T, Reisner E. Solar-driven reforming of solid waste for a sustainable future. Nat Sustain 2020;4(5):383–91.
[22] Bajpai H, Chauhan I, Salgaonkar KN, Mhamane NB, Gopinath CS. Biomass components toward $H_2$ and value-added products by sunlight-driven photocatalysis with electronically integrated $Au^{\delta-}$–$TiO_2$: concurrent utilization of electrons and holes. RSC Sustain 2023;1(3):481–93.
[23] Yang J, Wang D, Han H, Li C. Roles of cocatalysts in photocatalysis and photoelectrocatalysis. Acc Chem Res 2013;46(8):1900–9.
[24] Ran J, Zhang J, Yu J, Jaroniec M, Qiao SZ. Earth-abundant cocatalysts for semiconductor-based photocatalytic water splitting. Chem Soc Rev 2014;43(22):7787–812.
[25] Murdoch M, Waterhouse GIN, Nadeem MA, Metson JB, Keane MA, Howe RF, Llorca J, Idriss H. The effect of gold loading and particle size on photocatalytic hydrogen production from ethanol over $Au/TiO_2$ nanoparticles. Nat Chem 2011;3(6):489–92.
[26] Puga AV, Forneli A, García H, Corma A. Production of $H_2$ by ethanol photoreforming on $Au/TiO_2$. Adv Funct Mater 2014;24:241–8.
[27] Su R, Tiruvalam R, Logsdail AJ, He Q, Downing CA, Jensen MT, Dimitratos N, Kesavan L, Wells PP, Bechstein R, Jensen HH, Wendt S, Catlow CRA, Kiely CJ, Hutchings GJ, Besenbacher F. Designer titania-supported Au-Pd nanoparticles for efficient photocatalytic hydrogen production. ACS Nano 2014;8(4):3490–7.
[28] Al-Azri ZHN, AlOufi M, Chan A, Waterhouse GIN, Idriss H. Metal particle size effects on the photocatalytic hydrogen ion reduction. ACS Catal 2019;9(5):3946–58.
[29] Chen Y, Soler L, Cazorla C, Oliveras J, Bastús NG, Puntes VF, Llorca J. Facet-engineered $TiO_2$ drives photocatalytic activity and stability of supported noble metal clusters during $H_2$ evolution. Nat Commun 2023;14(1):6165.
[30] Bahruji H, Bowker M, Brookes C, Davies PR, Wawata I. The adsorption and reaction of alcohols on $TiO_2$ and $Pd/TiO_2$ catalysts. Appl Catal A-Gen 2013;454:66–73.
[31] Dessal C, Martínez L, Maheu C, Len T, Morfin F, Rousset JL, Puzenat E, Afanasiev P, Aouine M, Soler L, Llorca J, Piccolo L. Influence of Pt particle size and reaction phase on the photocatalytic performances of ultradispersed $Pt/TiO_2$ catalysts for hydrogen evolution. J Catal 2019;375:155–63.
[32] Liu L, Meira DM, Arenal R, Concepcion P, Puga AV, Corma A. Determination of the evolution of heterogeneous single metal atoms and nanoclusters under reaction conditions: which are the working catalytic sites? ACS Catal 2019;9(12):10626–39.
[33] Kondarides DI, Daskalaki VM, Patsoura A, Verykios XE. Hydrogen production by photo-induced reforming of biomass components and derivatives at ambient conditions. Catal Lett 2008;122:26–32.
[34] Patsoura A, Kondarides DI, Verykios XE. Photocatalytic degradation of organic pollutants with simultaneous production of hydrogen. Catal Today 2007;124:94–102.
[35] Gao C, Low J, Long R, Kong T, Zhu J, Xiong Y. Heterogeneous single-atom photocatalysts: fundamentals and applications. Chem Rev 2020;120(21):12175–216.
[36] Xue Z-H, Luan D, Zhang H, Lou XW. Single-atom catalysts for photocatalytic energy conversion. Joule 2022;6(1):92–133.
[37] Rigby K, Kim J-H. Deciphering the issue of single-atom catalyst stability. Current Opinion Chem Eng 2023;40:100921.
[38] Zhou X, Hwang I, Tomanec O, Fehn D, Mazare A, Zboril R, Meyer K, Schmuki P. Advanced photocatalysts: pinning single atom Co-catalysts on titania nanotubes. Adv Funct Mater 2021;31(30):2102843.
[39] Qin S, Will J, Kim H, Denisov N, Carl S, Spiecker E, Schmuki P. Single atoms in photocatalysis: low loading is good enough. ACS Energy Lett 2023;8(2):1209–14.
[40] Denisov N, Qin S, Will J, Vasiljevic BN, Skorodumova NV, Pašti IA, Sarma BB, Osuagwu B, Yokosawa T, Voss J, Wirth J, Spiecker E, Schmuki P. Light-induced

agglomeration of single-atom platinum in photocatalysis. Adv Mater 2023;35(5):2206569.
[41] Piccolo L, Afanasiev P, Morfin F, Len T, Dessal C, Rousset JL, Aouine M, Bourgain F, Aguilar-Tapia A, Proux O, Chen Y, Soler L, Llorca J. Operando X-ray absorption spectroscopy investigation of photocatalytic hydrogen evolution over ultradispersed Pt/$TiO_2$ catalysts. ACS Catal 2020;10(21):12696–705.
[42] Fornasiero P, Christoforidis KC. Photocatalysis for hydrogen production and $CO_2$ reduction: the case of copper-catalysts. ChemCatChem 2018;11(1):368–82.
[43] Montini T, Gombac V, Sordelli L, Delgado JJ, Chen X, Adami G, Fornasiero P. Nanostructured Cu/$TiO_2$ photocatalysts for $H_2$ production from ethanol and glycerol aqueous solutions. ChemCatChem 2011;3:574–7.
[44] Gombac V, Sordelli L, Montini T, Delgado JJ, Adamski A, Adami G, Cargnello M, Bernal S, Fornasiero P. $CuO_x$-$TiO_2$ photocatalysts for $H_2$ production from ethanol and glycerol solutions. J Phys Chem A 2010;114:3916–25.
[45] Kannan K, Gautam J, Chanda D, Meshesha MM, Jang SG, Yang BL. Two dimensional MAX supported copper oxide/nickel Oxide/MAX as an efficient and novel photocatalyst for hydrogen evolution. Int J Hydrogen Energy 2023;48(20):7273–83.
[46] Kannan K, Chanda D, Gautam J, Behera A, Meshesha MM, Gwon Jang S, Yang B. Hydrothermally synthesized mixed metal oxide nanocomposites for electrochemical water splitting and photocatalytic hydrogen production. Int J Hydrogen Energy 2023;48(93):36412–26.
[47] Trofimovaite R, Parlett CMA, Kumar S, Frattini L, Isaacs MA, Wilson K, Olivi L, Coulson B, Debgupta J, Douthwaite RE, Lee AF. Single atom Cu(I) promoted mesoporous titanias for photocatalytic Methyl Orange depollution and $H_2$ production. Appl Catal, B 2018;232:501–11.
[48] Lee B-H, Park S, Kim M, Sinha AK, Lee SC, Jung E, Chang WJ, Lee K-S, Kim JH, Cho S-P, Kim H, Nam KT, Hyeon T. Reversible and cooperative photoactivation of single-atom Cu/$TiO_2$ photocatalysts. Nat Mater 2019;18(6):620–6.
[49] Zhang Y, Zhao J, Wang H, Xiao B, Zhang W, Zhao X, Lv T, Thangamuthu M, Zhang J, Guo Y, Ma J, Lin L, Tang J, Huang R, Liu Q. Single-atom Cu anchored catalysts for photocatalytic renewable $H_2$ production with a quantum efficiency of 56. Nat Commun 2022;13(1):58.
[50] Petala A, Ioannidou E, Georgaka A, Bourikas K, Kondarides DI. Hysteresis phenomena and rate fluctuations under conditions of glycerol photo-reforming reaction over $CuO_x$/$TiO_2$ catalysts. Appl Catal, B 2015;178:201–9.
[51] Wang Z, Teramura K, Shishido T, Tanaka T. Characterization of Cu nanoparticles on $TiO_2$ photocatalysts fabricated by electroless plating method. Top Catal 2014;57(10–13):975–83.
[52] Ribao P, Alexandra Esteves M, Fernandes VR, Rivero MJ, Rangel CM, Ortiz I. Challenges arising from the use of $TiO_2$/rGO/Pt photocatalysts to produce hydrogen from crude glycerol compared to synthetic glycerol. Int J Hydrogen Energy 2019;44(53):28494–506.
[53] Esteves MA, Fresno F, Fernandes VR, Oropeza FE, de la Peña O'Shea VA, Rangel CM. $TiO_2$-reduced graphene oxide-Pt nanocomposites for the photogeneration of hydrogen from ethanol liquid and gas phases. Catal Today 2021;380:41–52.
[54] Spasiano D, Marotta R, Malato S, Fernandez-Ibañez P, Di Somma I. Solar photocatalysis: materials, reactors, some commercial, and pre-industrialized applications. A comprehensive approach. Appl Catal, B 2015;170–171:90–123.
[55] Bahnemann D. Photocatalytic water treatment: solar energy applications. Sol Energy 2004;77(5):445–59.
[56] Nalajala N, Salgaonkar KN, Chauhan I, Mekala SP, Gopinath CS. Aqueous methanol to formaldehyde and hydrogen on Pd/$TiO_2$ by photocatalysis in direct sunlight: structure dependent activity of nano-Pd and atomic Pt-coated counterparts. ACS Appl Energy Mater 2021;4(11):13347–60.
[57] Gopinath CS, Nalajala N. A scalable and thin film approach for solar hydrogen generation: a review on enhanced photocatalytic water splitting. J Mater Chem A 2021;9(3):1353–71.
[58] Puga A, Fattoruso D. Eur. Pat., EP21382740. 2021.
[59] Dahl M, Liu Y, Yin Y. Composite titanium dioxide nanomaterials. Chem Rev 2014;114(19):9853–89.
[60] Liu L, Corma A. Metal catalysts for heterogeneous catalysis: from single atoms to nanoclusters and nanoparticles. Chem Rev 2018;118(10):4981–5079.
[61] Imaoka T, Akanuma Y, Haruta N, Tsuchiya S, Ishihara K, Okayasu T, Chun W-J, Takahashi M, Yamamoto K. Platinum clusters with precise numbers of atoms for preparative-scale catalysis. Nat Commun 2017;8(1):688.
[62] Puga AV, Barka N, Imizcoz M. Simultaneous $H_2$ production and bleaching via solar photoreforming of model dye-polluted wastewaters on metal/titania. ChemCatChem 2021;13(6):1513–29.
[63] Jiang X, Fu X, Zhang L, Meng S, Chen S. Photocatalytic reforming of glycerol for $H_2$ evolution on Pt/$TiO_2$: fundamental understanding the effect of co-catalyst Pt and the Pt deposition route. J Mater Chem A 2015;3(5):2271–82.
[64] Bashir S, Wahab AK, Idriss H. Synergism and photocatalytic water splitting to hydrogen over M/$TiO_2$ catalysts: effect of initial particle size of $TiO_2$. Catal Today 2015;240:242–7.
[65] Wu Z, Li Y, Huang W. Size-dependent Pt-$TiO_2$ strong metal–support interaction. J Phys Chem Lett 2020;11(12):4603–7.
[66] Han B, Guo Y, Huang Y, Xi W, Xu J, Luo J, Qi H, Ren Y, Liu X, Qiao B, Zhang T. Strong metal–support interactions between Pt single atoms and $TiO_2$. Angew Chem, Int Ed 2020;59(29):11824–9.
[67] Wenderich K, Mul G. Methods, mechanism, and applications of photodeposition in photocatalysis: a review. Chem Rev 2016;116(23):14587–619.
[68] Imizcoz M, Puga AV. Optimising hydrogen production via solar acetic acid photoreforming on Cu/$TiO_2$. Catal Sci Technol 2019;9(5):1098–102.
[69] Hussein FH, Rudham R. Photocatalytic dehydrogenation of liquid alcohols by platinized anatase. J Chem Soc, Faraday Trans 1987;1(83):1631–9.
[70] Bajpai H, Nivedhitha TR, Dais E, Kanungo SS, Gopinath CS. Oxidative and selective C–C cleavage of glycerol to glycolaldehyde with atom-like Cu on Cu-$TiO_2$: photocatalytic water reduction with concurrent glycerol oxidation in sunlight. J Catal 2024;437:115644.
[71] Qian C, Liu H, Li H, Wang T, Wang S. Mesoporous TiO2 spheres with rich oxygen vacancies for enhanced photocatalytic hydrogen production. Int J Hydrogen Energy 2024;51:605–14.
[72] Kumar D, Mishra A, Shubham Hemant, Bhattacharjee S, Urkude RR, Ghosh B, Bhaumik A, Sinha AK, Sinha ASK, Amoli V. Highly asymmetric CuSA-ov-Ti3c atomic sites catalyst for unprecedented solar hydrogen generation. Adv Energy Mater 2024;14(32):2401964.
[73] Xiao B, Shen C, Luo Z, Li D, Zi B, Zhou T, Sun H, Chen M, Zhang J, Zhu Z, Liu F, Cui H, Liu Q. Modulating d-p-band electron coupling by N-doping for promoting CuSAs-N/TiO2 photocatalytic hydrogen evolution. Chem Eng J 2024;499:156331.
[74] Villachica-Llamosas JG, Ruiz-Aguirre A, Colón G, Peral J, Malato S. CuO–$TiO_2$ pilot-plant system performance for solar photocatalytic hydrogen production. Int J Hydrogen Energy 2024;51:1069–77.
[75] Maldonado MI, López-Martín A, Colón G, Peral J, Martínez-Costa JI, Malato S. Solar pilot plant scale hydrogen generation by irradiation of Cu/$TiO_2$ composites in presence of sacrificial electron donors. Appl Catal, B 2018;229:15–23.
[76] Villa K, Domènech X, Malato S, Maldonado MI, Peral J. Heterogeneous photocatalytic hydrogen generation in a solar pilot plant. Int J Hydrogen Energy 2013;38(29):12718–24.
[77] Arzate Salgado SY, Ramírez Zamora RM, Zanella R, Peral J, Malato S, Maldonado MI. Photocatalytic hydrogen production in a solar pilot plant using a Au/$TiO_2$ photo catalyst. Int J Hydrogen Energy 2016;41(28):11933–40.
[78] Al-Azri ZHN, Chen W-T, Chan A, Jovic V, Ina T, Idriss H, Waterhouse GIN. The roles of metal co-catalysts and reaction media in photocatalytic hydrogen production: performance evaluation of M/$TiO_2$ photocatalysts (M = Pd, Pt, Au) in different alcohol-water mixtures. J Catal 2015;329:355–67.
[79] Zhang N, Han C, Xu Y-J, Foley Iv JJ, Zhang D, Codrington J, Gray SK, Sun Y. Near-field dielectric scattering promotes optical absorption by platinum nanoparticles. Nat Photonics 2016;10(7):473–82.
[80] Huang BS, Chang FY, Wey MY. Photocatalytic properties of redox-treated Pt/$TiO_2$ photocatalysts for $H_2$ production from an aqueous methanol solution. Int J Hydrogen Energy 2010;35(15):7699–705.
[81] Polliotto V, Livraghi S, Krukowska A, Dozzi MV, Zaleska-Medynska A, Selli E, Giamello E. Copper-modified $TiO_2$ and $ZrTiO_4$: Cu oxidation state evolution during photocatalytic hydrogen production. ACS Appl Mater Interfaces 2018;10(33):27745–56.
[82] Navarro RM, Arenales J, Vaquero F, Gonzalez ID, Fierro JLG. The effect of Pt characteristics on the photoactivity of Pt/$TiO_2$ for hydrogen production from ethanol. Catal Today 2013;210:33–8.
[83] Zhou X, Wang Y, Denisov N, Kim H, Kim J, Will J, Spiecker E, Vaskevich A, Schmuki P. Pt single atoms loaded on thin-layer TiO2 electrodes: electrochemical and photocatalytic features. Small 2024;20(47):e2404064.
[84] Schweinberger FF, Berr MJ, Döblinger M, Wolff C, Sanwald KE, Crampton AS, Ridge CJ, Jäckel F, Feldmann J, Tschurl M, Heiz U. Cluster size effects in the photocatalytic hydrogen evolution reaction. J Am Chem Soc 2013;135(36):13262–5.
[85] Wang D, Liu Z-P, Yang W-M. Revealing the size effect of platinum cocatalyst for photocatalytic hydrogen evolution on $TiO_2$ support: a DFT study. ACS Catal 2018;8(8):7270–8.
[86] Qin S, Denisov N, Sarma BB, Hwang I, Doronkin DE, Tomanec O, Kment S, Schmuki P. Pt single atoms on $TiO_2$ polymorphs—minimum loading with a maximized photocatalytic efficiency. Adv Mater Interfac 2022;9(22):2200808.
[87] López CR, Melián EP, Ortega Méndez JA, Santiago DE, Doña Rodríguez JM, González Díaz O. Comparative study of alcohols as sacrificial agents in $H_2$ production by heterogeneous photocatalysis using Pt/$TiO_2$ catalysts. J Photochem Photobiol 2015;312:45–54. A.
[88] Kawai M, Kawai T, Naito S, Tamaru K. The mechanism of photocatalytic reaction over platinum/titanium dioxide: production of molecular hydrogen and aldehyde from gaseous alcohol and water. Chem Phys Lett 1984;110:58–62.
[89] Bamwenda GR, Tsubota S, Nakamura T, Haruta M. Photoassisted hydrogen production from a water-ethanol solution: a comparison of activities of Au-$TiO_2$ and Pt-$TiO_2$. J Photochem Photobiol 1995;89:177–89. A.
[90] Clarizia L, Apuzzo J, Di Somma I, Marotta R, Andreozzi R. Selective photo-oxidation of ethanol to acetaldehyde and acetic acid in water in presence of $TiO_2$ and cupric ions under UV–simulated solar radiation. Chem Eng J 2019;361:1524–34.
[91] Karimi Estahbanati MR, Babin A, Feilizadeh M, Nayernia Z, Mahinpey N, Iliuta MC. Photocatalytic conversion of alcohols to hydrogen and carbon-containing products: a cleaner alcohol valorization approach. J Clean Prod 2021;318:128546.
[92] Nomikos GN, Panagiotopoulou P, Kondarides DI, Verykios XE. Kinetic and mechanistic study of the photocatalytic reforming of methanol over Pt/$TiO_2$ catalyst. Appl Catal, B 2014;146:249–57.
[93] Gu Q, Fu X, Wang X, Chen S, Leung DYC, Xie X. Photocatalytic reforming of C3-polyols for $H_2$ production. Part II. FTIR study on the adsorption and photocatalytic reforming reaction of 2-propanol on Pt/$TiO_2$. Appl Catal, B 2011;106:689–96.
[94] Coronado JM, Kataoka S, Tejedor-Tejedor I, Anderson MA. Dynamic phenomena during the photocatalytic oxidation of ethanol and acetone over nanocrystalline

$TiO_2$: simultaneous FTIR analysis of gas and surface species. J Catal 2003;219:219–30.
[95] Gong D, Subramaniam VP, Highfield JG, Tang Y, Lai Y, Chen Z. In situ mechanistic investigation at the liquid/solid interface by attenuated total reflectance FTIR: ethanol photo-oxidation over pristine and platinized $TiO_2$ (P25). ACS Catal 2011;1(8):864–71.
[96] Mino L, Spoto G, Ferrari AM. $CO_2$ capture by $TiO_2$ anatase surfaces: a combined DFT and FTIR study. J Phys Chem C 2014;118(43):25016–26.
[97] Mahdavi-Shakib A, Arce-Ramos JM, Austin RN, Schwartz TJ, Grabow LC, Frederick BG. Frequencies and thermal stability of isolated surface hydroxyls on pyrogenic $TiO_2$ nanoparticles. J Phys Chem C 2019;123(40):24533–48.
[98] Lan L, Daly H, Sung R, Tuna F, Skillen N, Robertson PKJ, Hardacre C, Fan X. Mechanistic study of glucose photoreforming over $TiO_2$-based catalysts for $H_2$ production. ACS Catal 2023;13(13):8574–87.
[99] Ekström GN, McQuillan AJ. In situ infrared spectroscopy of glyoxylic acid adsorption and photocatalysis on $TiO_2$ in aqueous solution. J Phys Chem B 1999;103(48):10562–5.
[100] Strataki N, Bekiari V, Kondarides DI, Lianos P. Hydrogen production by photocatalytic alcohol reforming employing highly efficient nanocrystalline titania films. Appl Catal, B 2007;77:184–9.